


Unsteady Inherent Convective Mixing in Thermal-Energy-Storage Systems during Standby Periods

Henning Otto¹, Clemens Naumann¹, Christian Odenthal², and Christian Cierpka^{1,*}

¹*Institute of Thermodynamics and Fluid Mechanics, Technische Universität Ilmenau, Am Helmholtzring 1 Ilmenau 98693, Germany*

²*Institute of Engineering Thermodynamics, German Aerospace Center (DLR), Linder Höhe, Köln 51147, Germany*

 (Received 3 April 2023; revised 25 July 2023; accepted 4 August 2023; published 2 October 2023)

Recent studies on the flow phenomena in stratified thermal-energy-storage (TES) systems have shown that heat conduction from the hot upper fluid layer through the vertical tank sidewall into the lower cold fluid layer leads to counterdirected wall jets adjacent to the vertical sidewalls. It was shown that these phenomena destroyed half of the total exergy content in less than a tenth of the storage time constant of a 2-m³ stratified TES system. This paper investigates short-term fluctuations of the wall jets since these fluctuations can potentially mix the hot and cold zones of the thermal stratification that are separated by the thermocline region. Using particle-image velocimetry measurements in two regions of a TES model experiment (near-wall region and far-field region) and analyzing the frequency content of the velocity fields revealed characteristic oscillations for different regions. In the near-wall region, observed fluctuations agreed well with an adjusted boundary layer frequency from the literature, showing that the wall jet is transitioning from laminar to turbulent flow. In the far-field region, the oscillations are related to the Brunt-Väisälä frequency. It is shown that the fluctuations from the boundaries of the thermocline region are most dominant and propagate into deeper regions of the thermocline. A comparison to data from the large-scale test facility for thermal energy storage in molten salt at the German Aerospace Center in Cologne showed good agreement. The consensus between the two experiments proves firstly that a small-scale model experiment with water as a storage liquid can be used to analyze the physical phenomena of large-scale molten salt storage facilities and secondly that these fluctuations are relevant for exergy destruction in real-scale TES.

DOI: [10.1103/PRXEnergy.2.043001](https://doi.org/10.1103/PRXEnergy.2.043001)

I. INTRODUCTION

It is widely known that renewable energy sources are of major importance in opposing climate change by replacing conventional power plants that use fossil fuels [1]. Thermal-energy-storage (TES) systems are one promising solution to solve the energy storage problem that most renewable power plants have due to their intermittent energy supply [2]. Currently, there are only limited CO₂-neutral technological solutions available to solve this issue, like pumped hydro energy storage (PHS), adiabatic compressed air storage, and chemical storage by hydrogen. TES, as one of the key components of Carnot batteries

[3–7], may also play a major role in heat storage for industrial and home use, especially when it comes to seasonal storage technologies that store energy harvested in the warmer period of the year. Therefore, TES systems have the potential to be used as a seasonal energy storage system for both electric energy [8] and heat [9]. Moreover, they are suitable for large-scale energy management besides PHS and large-scale compressed air energy storage [2,8], and have the advantage of lower investment costs. On a smaller scale, like the application in microgrids, TES systems are also suitable and provide the long storage times in comparison to other methods [10]. In general, TES systems are separated based on their storage principle into sensible heat, latent heat, and thermochemical TES systems, which have already been investigated extensively in the literature regarding their possible applications [7,11–15]. A common type of TES is the single-tank stratified TES that uses liquids like water or molten salt as a storage material. In such stratified TES systems, the temperature dependency of the storage mediums' density is utilized to provide a hot reservoir at the top of the tank that is separated by the so-called

*christian.cierpka@tu-ilmenau.de;

<https://www.tu-ilmenau.de/ttd>

Published by the American Physical Society under the terms of the [Creative Commons Attribution 4.0 International](https://creativecommons.org/licenses/by/4.0/) license. Further distribution of this work must maintain attribution to the author(s) and the published article's title, journal citation, and DOI.

thermocline (the region of a temperature step) from the cold reservoir at the bottom. Efficient use of such stratified systems is only possible if the two reservoirs stay separated by preventing convective mixing of the two layers. One main advantage of stratified TES is low investment costs [16] while also offering a long lifetime, low maintenance efforts, and environmentally safe operation due to nontoxic storage fluids.

For this reason, stratified TES systems have already been investigated extensively, especially in terms of efficient charging and discharging processes to prevent the mixing of the hot and the cold reservoirs [17–26]. However, less attention was drawn to the standby period of stratified TES in the past, which becomes increasingly relevant for long-term storage. During those standby periods, the stratification is generally stable, but the heat conducting sidewall of typical storage tanks can lead to unwanted natural convection in the near-wall region and thus to mixing of the fluid layers. In a recent study by the authors, it was shown that the high thermal conductivity of the sidewall leads to decreasing exergy efficiency of the TES caused by convective mixing of the two layers and the associated entropy production. In a well-insulated 2-m³ stratified TES system, the vertical heat transfer dominates, and these phenomena destroyed half of the total exergy content in less than one-tenth of the storage time constant [27]. As long storage times are promoted by better insulation, these effects become more important for future large-scale TES applications. Furthermore, the flow structures of the natural convection along the vertical sidewalls were investigated by means of time-averaged particle-image velocimetry (PIV) measurements [28]. Overall, it was shown that two large-scale circulations form in the storage facility due to a heat flux from the hot fluid layer into the sidewall, downwards, and then into the cold layer. In the near-wall region, the flow is characterized by the highest velocities as the driving heat flux takes place in this position, while the flow in the far field of the wall is just a result of mass conservation. Figure 1 shows a schematic sketch of the described flow structures.

During the time-averaged flow investigations, it was also noticed that in the upper, hot part of the model TES, the vertical wall jet is characterized by a thinner horizontal extent and higher velocities compared to the lower wall jet in the bottom. The reason for that was the change in the temperature-dependent fluid properties, where the viscosity of water decreases by nearly half between the cold bottom temperature and the hot upper part for typical storage temperatures of nonpressurized systems. Consequently, it was unsurprising that the upper wall-jet's flow was rather unsteady, showing strong velocity fluctuations even though it did not seem completely turbulent. However, previous studies have not captured these unsteady phenomena in a detailed temporal survey. For this reason, this paper aims to investigate both the fluctuations of the

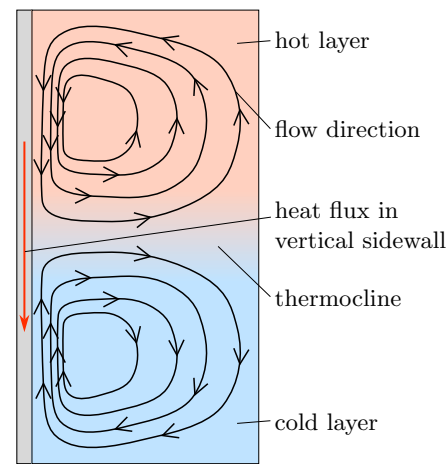


FIG. 1. Depiction of the overall flow structures inside the model experiment of stratified TES due to the influence of a vertical, highly heat-conducting sidewall.

upper wall jet and its influence on the flow conditions in the far field of the vertical wall.

The paper is structured as follows. Section II reviews the relevant literature on fluctuations of natural convection in TES and fundamental research in the field of instabilities in stratified fluids. Then, Sec. III describes the experimental setup and the measurement procedure for the measurements of the fluctuating flow. After that, the results are presented in Sec. IV, and in Sec. V a comparison to a real-scale TES facility using molten salt as the storage fluid is conducted. Finally, the main findings and conclusions are summarized in Sec. VI.

II. STATE OF THE ART ON INSTABILITIES IN THERMAL ENERGY STORAGE AND STRATIFIED FLUIDS

A. Fluctuations of the wall jet

Generally, the fluid mechanical phenomena of near-wall convection inside TES is a relatively rarely investigated topic. In the literature, there are some studies on the influence of axial wall conduction, meaning the heat flux from the hot upper layer to the lower cold layer through the vertical tank wall. For example, Shyu and Hsieh [29] investigated the stability of thermal stratification in an enclosure with a vertical heat-conducting sidewall with either no insulation, outer, or inner insulation. They found that the inner insulation results in the longest time spans of stable stratification due to the suppression of heat conduction from top to bottom. Shyu *et al.* [30] found that axial wall conduction decreases the stratification of a TES system, and better outer insulation lowers the heat loss to the surrounding but accelerates the destruction of the stratification. Moreover, they found that natural convection due to axial heat conduction leads to recirculation of the fluid in the tank (similar to what is shown in Fig. 1), leading

to increased effective fluid conduction by a factor of 2–3. Nelson *et al.* [31] used a one-dimensional conjugate heat conduction model in a parameter study on thermal stratification in TES. They found that axial wall conduction is increased due to exterior wall insulation, which leads to enhanced stratification degradation. Papanicolaou and Belessiotis [32] numerically studied the standby behavior of an underground TES system initially filled with isothermal hot water and showed that stratification forms quickly before it decays again. This decay hints at internal heat conduction through the fluid, the sidewalls, or both.

Even though the studies mentioned above agree that axial wall conduction negatively impacts the stratification of TES, the effects of convective fluid mixing in the thermocline region were not discussed in detail. However, natural convection along a vertical wall has been a fundamental topic in fluid mechanics for several decades, and many studies on the topic have been published. Regarding fluctuations in the velocity boundary layer of a vertical wall in stratified media, there are early studies, e.g., from Jaluria and Gebhart [33], who investigated vertical convection in a stratified medium with a uniform heat flux dissipated from the wall. They found that the thermal stratification stabilizes the wall jet since perturbations destabilize the velocity boundary layer further downstream. Moreover, they found that the transition to turbulence is delayed by the ambient stratification of the fluid. Patterson and Armfield [34] investigated the flow physics in a cavity with one heated and one cooled vertical sidewall. They found that the vertical convective flow is subject to two kinds of boundary layer instability, with one being characterized by high-frequency fluctuations that might be related to the transition to turbulence.

Later, Zhao *et al.* [35] numerically investigated how the stability of a natural convective boundary layer of an isothermal, heated plate reacts to perturbations. It was shown that small disturbances of the boundary layer could lead to turbulent motion, in which case the boundary layer starts oscillating with a characteristic frequency for which they provided an empirical formulation. Furthermore, this oscillation increases the heat flux between the fluid and wall by 46% in that specific case. In a later study, they experimentally investigated the natural boundary layer in a model experiment using PIV measurements [36]. In this second study, they confirmed the empirical formulation for the characteristic frequency, that is,

$$f_{\text{wj}} = 0.0136 \left(\frac{g\beta\Delta\vartheta}{\kappa} \right)^{2/3} \nu^{1/3}, \quad (1)$$

where g is the acceleration due to gravity, β is the volumetric expansion coefficient of the fluid, $\Delta\vartheta$ is the temperature difference between the vertical wall and the fluid in the far field, κ is the thermal diffusivity of the fluid, and ν is the fluid's kinematic viscosity. The relation $f \sim \text{Ra}^{2/3}$,

on which the empirical formulation of Zhao *et al.* [36] is based, was initially stated by Gebhart and Mahajan [37] regarding natural convection flow at a vertical side wall.

B. Fluctuations of the far-field region

In the late 1990s van Berkel [38] and in the early 2000s van Berkel *et al.* [17] investigated the mixing behavior of stratified TES. Using a model experiment for flow visualizations with a fluorescent dye and quantitative measurements by particle tracking velocimetry showed Kelvin-Helmholtz instabilities near the inlet jet, which was decelerated by the thermocline, leading to a swaying motion of the jet at a certain frequency. The same frequency was also found in an oscillation of the thermocline and was related to the jet's motion.

Ratnu and Manu [39] numerically investigated the unsteady behavior of stratified TES by disturbing a model system of a stratified TES with short inlet flows of cold fluid. That inlet flows rolled up when approaching the thermocline, leading to different flow structures. The interface in the thermocline region was found to be subject to standing-wave oscillations near the buoyancy frequency [also referred to as the Brunt-Väisälä frequency (BVF)]. Moreover, the dominant frequencies found in the spectra of time-series data reduced with increasing thermocline thickness and hence reduced temperature gradients.

Advaith *et al.* [25] also investigated the impingement of a vortex ring on a thermocline with the motivation for a better understanding of the physical processes in stratified TES of concentrated solar power. They found that the impingement of the vortex ring can cause oscillations of the density interface with frequencies near the BVF.

The studies that inspired Advaith *et al.* [25] to their investigations were performed by Manu *et al.* [23,40] and Tinaikar *et al.* [24], who numerically investigated the influence of the inflow in a stratified TES system from different aspects, respectively. Manu *et al.* [23,40] found that the thermocline is stable for Earth's gravity compared to lower gravitational acceleration, and the system showed Rayleigh-Taylor instabilities between the fluids of different temperatures. Moreover, Tinaikar *et al.* [24] found that the impingement of vortices on the thermocline led to oscillations with frequencies below the BVF.

As the previous examples from the literature have shown, it seems that the BVF is an important parameter in the case of flow instabilities in density-stratified media. Generally, the BVF describes the frequency at which a stratified fluid oscillates if fluid parcels are vertically displaced from their original position. The reason for this oscillation is the change between potential and kinetic energy since the displaced fluid parcel gains potential energy (either positive or negative) when it is moved to an environment with a different density and releases this into kinetic energy when it starts moving back to its original

position. The BVF is highly important for describing such systems in the scientific fields of oceanography and meteorology. However, it can also occur in smaller, technical systems. In these applications, the BVF can be calculated as

$$f_{\text{BV}} = \frac{N}{2\pi} = \frac{1}{2\pi} \sqrt{-\frac{g}{\rho_0} \frac{d\rho}{dy}}, \quad (2)$$

where N is the BVF in units of radians and f_{BV} the BVF in units of hertz, g is the acceleration due to gravity, ρ_0 is a reference density of the fluid, and $d\rho/dy$ is the vertical density gradient.

III. EXPERIMENTAL SETUP

A. Model experiment

Figure 2 shows a schematic of the experimental setup used for this study, consisting of a model experiment and temperature and velocity measuring techniques. The model experiment is a rectangular polycarbonate cell with height $H = 750$ mm on a square base with a width $W = 375$ mm. On one side of the cell, an aluminum wall of 10-mm thickness can be inserted to mimic a vertical tank sidewall of a TES system with high thermal diffusivity

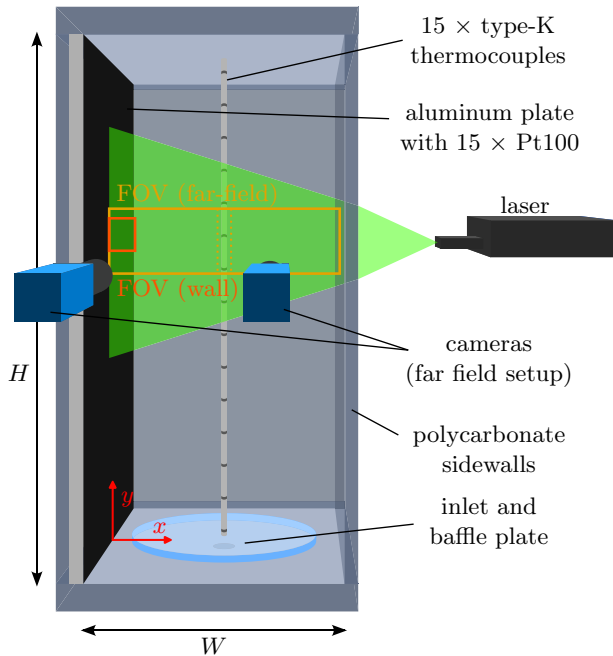


FIG. 2. Model experiment including the PIV system for flow measurements in the near-wall region and in the far field of the wall. The shown camera setup corresponds to the far-field measurement consisting of two adjacent cameras, while in the wall measurement, only one camera in combination with an objective lens with higher magnification is used. The differently colored rectangles show the corresponding fields of view (FOVs) of the two measurements.

($\kappa_{\text{Al}} = 104.4 \text{ m}^2 \text{ s}^{-1}$). In a previous study it was shown that the high thermal conductivity of the aluminum plate can compensate for the lower storage time constant and the lower storage height of the model experiment so that the exergetic decay is similar to that of a 2-m³ stratified TES system with a steel sidewall on a nondimensional time scale [27]. The model experiment can be filled from below through an inlet in the bottom panel covered by a circular baffle plate placed 10 mm above the inlet to prevent disturbing flow and, thus, mixing the thermally stratified fluid during filling. The thermal stratification is produced by filling half of the experiment's total volume with hot water using a flow heater and pushing the hot water to the top by filling the lower half with cold water from a cooled reservoir, bypassing the flow heater. Compared to the vertical aluminum plate, the water has much lower thermal diffusivity ($\kappa_{\text{W}} = 0.13 \text{ m}^2 \text{ s}^{-1}$), so the aluminum plate forms a thermal bridge between the stratification's hot upper layer and the lower cold layer.

During an experiment, the temperature distribution in both the aluminum plate and the water can be monitored using temperature sensors. For this reason, 15 Pt100 resistance thermometers [class AA with a tolerance of $\pm(0.1 \text{ K} + 0.0017\vartheta_{\text{W}})$, where ϑ_{W} is the water temperature in degrees Celsius] are equally distributed over the height in the inside of the aluminum plate. The water temperature is measured using 15 thermocouples (type K with an absolute tolerance of $\pm 0.1 \text{ K}$ after recalibration) that are attached to the vertical rod placed in the middle of the model experiment. Since the later evaluations of the water temperature rely mostly on the relative uncertainty of the thermocouples, this was also determined with the result that the standard deviation is in a range of $\sigma = \pm 0.02 \text{ K}$, which agrees well with the results of Yen Kee *et al.* [41], who found their thermocouples to have a relative uncertainty of $2\sigma = \pm 0.014 \text{ K}$ when the temperature was measured in a metal block. Moreover, an asymmetric logistic function is used to fit both the vertical wall temperature profile and the vertical water temperature profile. Details on the used fit function can be found in Otto and Cierpka [28].

B. Flow measurements—procedure and evaluation

Particle-image velocimetry offers the ability to perform high-resolution velocity measurements in a large field of view, including measurements close to walls [42,43]. The long-term PIV experiments were performed in different measurement positions to investigate the flow behavior in the model experiment. The long-term experiments covered 40 min starting 5 min after the ending of the filling process. This 5-min delay was necessary to calm initial flow disturbances from the filling process. The setup differed slightly, depending on the measurement position. The first measurement position (in the following referred to as the

wall measurement) is in the near-wall region. It covers a relatively small field of view (FOV) since the wall jet has high velocity gradients, requiring a high spatial resolution to be measured accurately. The second measurement position (*far-field measurement*) focuses on the far-field flow phenomena that the wall jet might induce. Therefore, it covers the entire width of the measuring cell using two adjacent cameras for an extended FOV in the horizontal direction. This increases the field of view while simultaneously maintaining a reasonable spatial resolution. The cameras used were sCMOS cameras (Imager sCMOS, LaVision) with a sensor resolution of 2560×2160 px, and, depending on the measurement position, equipped with an objective lens of 100-mm focal length (Milvius 2/100M, Zeiss) or 50-mm focal length [Planar T14/50 (4), Zeiss] for the wall and the far-field measurements, respectively. For the illumination of the measurement plane, a Nd:YAG double-pulse laser (Evergreen, Quantel Laser) was used, providing light pulses at a wavelength of 532 nm with pulse energy set to 20 mJ. The resulting light sheet was vertical, perpendicular to the aluminum wall at half of the depth of the measuring cell. The tracer particles used for the PIV measurements were PMMA particles with a diameter in the range $1 \leq d_p \leq 20 \mu\text{m}$ and a density of $\rho_p \approx 1170 \text{ kg m}^{-3}$ (DANTEC DYNAMICS). Since the particles were dyed with a fluorescent dye (rhodamine B) and the cameras' lenses were equipped with optical filters, reflections from the surfaces within the experiment could be eliminated, and only the emitted light from the particles was visible on the final camera images. The described PIV setup and the camera setup of the far-field measurement are shown in Fig. 2.

Table I lists the most important parameters of the PIV measurements. Different evaluation procedures for the PIV measurements were used depending on the measurement position. For the near-wall measurement, a combination of single frame (SF) evaluation in regions within the FOV with low velocities and double frame (DF) evaluation in regions with higher velocities was used. The threshold velocity under which the SF and above which the DF evaluation was used corresponds to a pixel displacement of 1/4 of the initial interrogation window size and

is $u_{\text{th}} = 1.98 \text{ mm s}^{-1}$. A more detailed description of the exact evaluation procedure can be found in Ref. [28]. The time difference between the two images is chosen according to the specific position within the FOV, either $\Delta t_{\text{w,SF}} = 1/F_{\text{s,w}}$ (for SF evaluation, where $F_{\text{s,w}}$ is the sampling frequency) or $\Delta t_{\text{w,DF}} = \delta t_{\text{w}}$ (for DF evaluation, where δt_{w} is the pulse delay of the laser). For the far-field measurement, only the single frame recording and evaluation procedure was used since flow velocities were relatively low. The spatial resolutions are the results of the calibration procedure performed before the measurements and are provided in Table I. The dynamic spatial range can be calculated by dividing the sensor size (in pixels) by the size of the interrogation window size, which was, in both measurements, 16 px for the final evaluation step. The vector spatial resolution gives the length in the vector field represented by one vector. The dynamic velocity range is the ratio between the maximum pixel displacement of the cross-correlations and the minimum resolvable pixel displacement (which is here assumed to be $\delta x = 0.1$ px) [44,45]. Finally, the velocity uncertainty was estimated by $\delta u = \delta x/D_R \cdot \Delta t$. Therefore, in the case of the wall measurement, the velocity uncertainty depends on the position and whether the SF or DF evaluation method was used.

IV. RESULTS OF THE PARTICLE-IMAGE VELOCIMETRY MEASUREMENT

At first, an overview of the two performed PIV measurements is given as a basis to be analyzed more deeply in the following. Therefore, Fig. 3 shows the results of the near-wall measurement. In Fig. 3(a) a snapshot of the vertical velocity component v is shown. The blue area on the left side shows the vertical wall jet in a downward direction. At the time of this snapshot, it features a flow fluctuation indicated by the thicker parts in the region between $480 \leq y \leq 510$ mm. An exemplary time evolution of this fluctuation is shown in Fig. 8 of Appendix A, which shows a vortex passing through the FOV from top to bottom close to the sidewall. The right side adjacent to the wall jet indicates the flow reversal due to temperature defects in the thermal boundary layer (see Ref. [28] for more details).

TABLE I. Details of the used PIV settings and the resulting resolutions of time, space, and velocity.

Parameter	Wall		Far field	
	Variable	Value	Variable	Value
Sampling frequency in hertz	$F_{\text{s,w}}$	7	$F_{\text{s,f}}$	0.5
Time difference in milliseconds	Δt_{w}	143 or 19.85	Δt_{f}	2000
Image resolution in px/mm	$D_{\text{R,w}}$	56.508	$D_{\text{R,w}}$	11.663
Dynamic spatial range	DSR_{w}	160	DSR_{f}	160
Vector spatial resolution in millimeters	Δx_{w}	0.28	Δx_{f}	1.37
Dynamic velocity range	DVR_{w}	80	DVR_{f}	160
Velocity uncertainty in mm/s	δu_{w}	0.012 or 0.089	δu_{f}	0.004

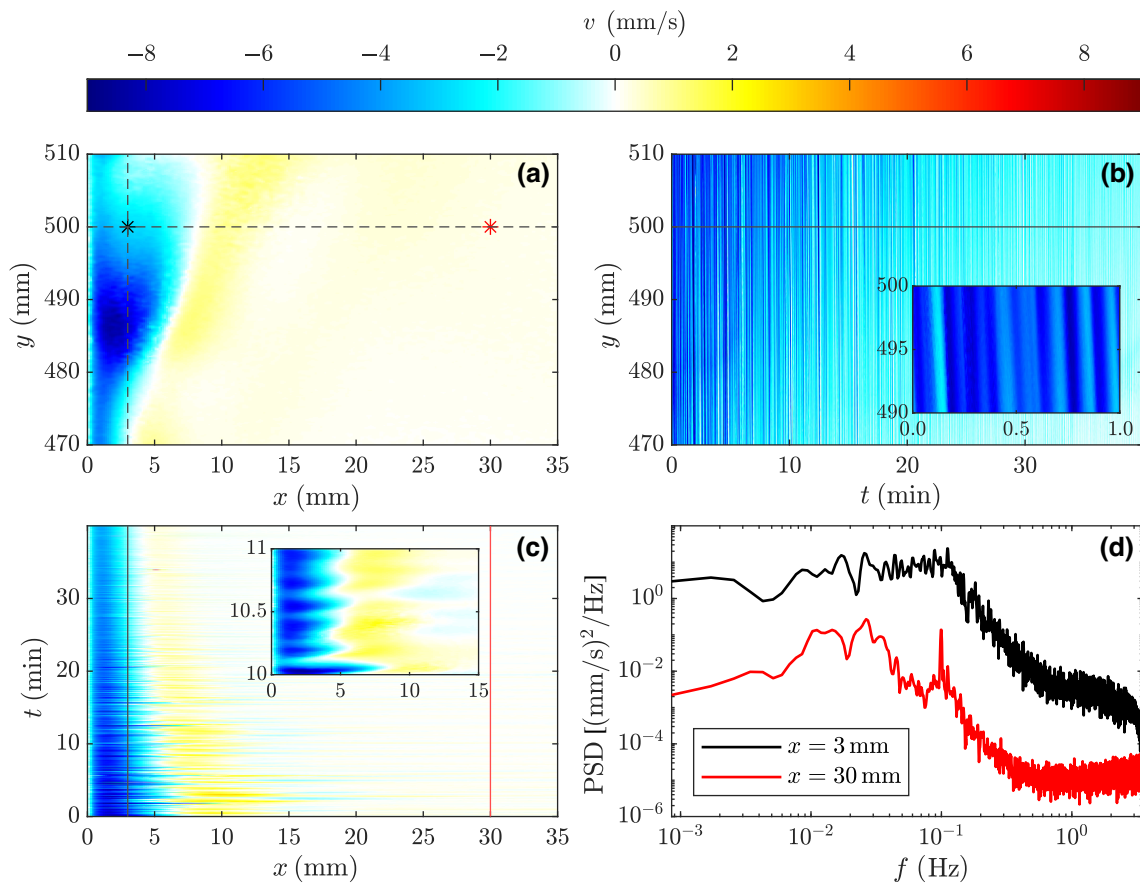


FIG. 3. (a) Snapshot of the far-field PIV result showing the near-wall measurement's vertical velocity component v . (b) Space-time plot of v along the vertical line at $x = 3$ mm [indicated by a dashed line in (a)]. (c) Space-time plot along the horizontal line at $y = 500$ mm [also indicated by a dashed line in (a)]. (d) Power spectral densities (PSDs) of two time series of v at two different distances to the vertical sidewall for a height of $y = 500$ mm. The time series are indicated as star markers or solid lines by their colors in the other subfigures.

Figure 3(b) shows a space-time plot of v along the vertical axis at $x = 3$ mm indicated by a dashed line in (a). The streak pattern shows flow fluctuations since each specific flow structure is represented by one color, and the colors constantly change over time, forming the streak pattern. In the inserted and enlarged plot, one can see that the streak pattern is slightly tilted so that it points from the top left to the bottom right. This slope indicates that the fluctuating flow structures are moving from the top over time to the bottom, keeping their specific color. Moreover, it can be seen that the magnitude of the flow velocity decreases over time, which was expected since the heat flux that drives the buoyancy-induced flow must also decrease over time while the entire system develops toward the equilibrium state.

Figure 3(c) also shows a space-time plot but now takes the velocity from the horizontal axis at $y = 500$ mm, indicated by a dashed line in Fig. 3(a). Here, one can see the temporal development of the wall-jet thickness decreasing over time. Like in Fig. 3(b), one can also see the temporal fluctuations even though the streak pattern looks different,

and a distinct slope of the streaks cannot be seen in the enlarged view. Therefore, the flow structures do not seem to have a specific horizontal movement.

Since Figs. 3(b) and 3(c) have revealed flow fluctuations over the entire measurement period with seemingly periodic behavior because the streak width stays relatively constant over time, Fig. 3(d) shows both time series' power spectral density (PSD). Star markers indicate the positions of those time series in Fig. 3(a), and lines indicate them in Figs. 3(b) and 3(c).

The black spectrum at $x = 3$ mm has its maximum at a frequency of $f = 1.1 \times 10^{-1}$ Hz. The spectrum drastically decays from this point towards higher frequencies, indicating that flow structures at such frequencies occur regularly. However, on the left side of the peak, the spectrum stays at a nearly constant power density, indicating that the occurring flow fluctuations include many different frequencies in a range $10^{-2} \leq f \leq 1.1 \times 10^{-1}$ Hz. A more detailed investigation of this plateau region was performed by splitting the underlying time series into four equally

long parts and calculating four subspectra (see Fig. 9 in Appendix B). The four subspectra reveal that, in the beginning, there is no dominant frequency but a similar plateau in the frequency range mentioned earlier. However, after roughly 25 min the plateau starts disappearing and a clear frequency peak at $f \approx 1.1 \times 10^{-1}$ Hz forms.

The red spectrum corresponding to a wall distance of $x = 30$ mm shows a slightly different behavior since two distinct peaks can be found in the spectrum. The first and highest peak can be found at $f = 2.6 \times 10^{-2}$ Hz. The second distinct peak with a very similar height is located at $f = 1 \times 10^{-1}$ Hz, nearly the same frequency as the peak in the black spectrum. Because of this observation, it can be assumed that the two distinct peaks have two different physical origins. Furthermore, the dominant peak in the red spectrum can be found at lower frequencies, while the dominant peak in the black spectrum is in the higher frequency range. Therefore, it can be assumed that the lower frequency originates from a certain flow structure of the far field while the higher frequency originates from the wall jet. However, this assumption needs further investigation.

For this reason, Fig. 4 shows the results of the PIV measurement in the far field using the same evaluation as for the wall measurement in Fig. 3. Therefore, Fig. 4(a) shows a snapshot of the horizontal velocity component u of the far-field measurement since, in this region, the main flow is in a horizontal direction. The very left and right parts are masked out (gray areas) since higher velocities were present in those regions that could not be resolved by the sampling frequency used (see Table I). The snapshot shows that the water streams to the right in nearly the entire FOV due to the positive velocity values. Only some smaller areas show slightly negative values, and overall the flow seems to be faster in the right half of the measuring cell, indicated by the orange and red regions. The reason for that phenomenon is unclear from this measurement. However, it is assumed to be related to a three-dimensional flow structure that forms to compensate for the mass flow inside the vertical wall jet. However, this paper aims not to investigate the overall flow structures but flow fluctuations, which are independent of the mean flow and, therefore, more independent of the specific geometry of the vessel.

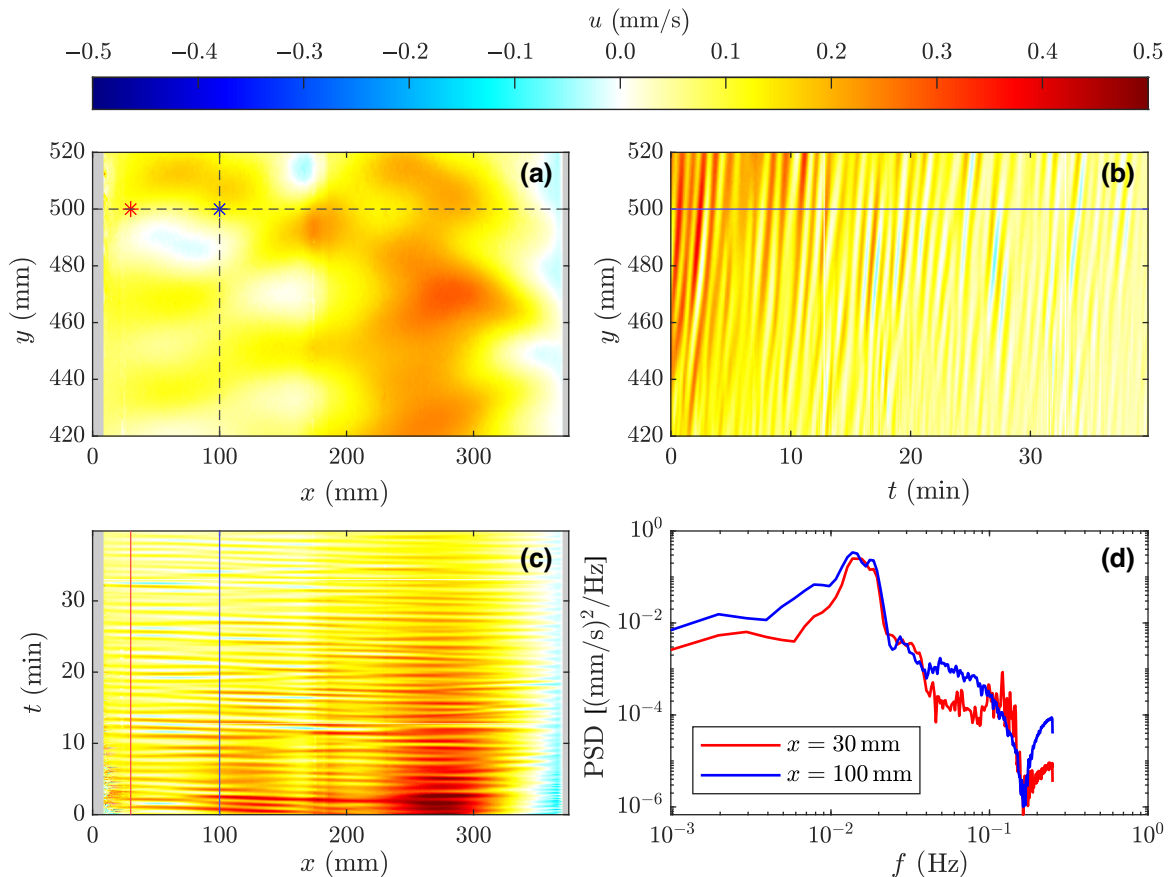


FIG. 4. (a) Snapshot of the far-field PIV result showing the horizontal velocity component u . The left and right borders of the field of view are masked in gray since velocities in those regions were too high to be properly resolved. (b) Space-time plot of u along the vertical line at $x = 100$ mm [indicated by a dashed line in (a)]. (c) Space-time plot along the horizontal line at $y = 500$ mm [also indicated by a dashed line in (a)]. (d) PSDs of two time series of u at two different distances to the vertical sidewall for a height of $y = 500$ mm. The time series are indicated by their colors in the other subfigures.

Figure 4(b) shows a space-time plot along the vertical dashed line in Fig. 4(a). In this plot, u is almost solely positive, meaning that the main flow streams in a wall-normal direction during the entire measurement. Moreover, the magnitude of the flow decreases over time, which is in good agreement with the flow of the wall jet that also slows down over time. Another interesting feature in this plot is that a streak pattern is again noticeable, showing periodic fluctuations in the flow. In contrast to the pattern shown in Fig. 3(b), the flow here fluctuates much slower since the streaks appear thicker. The slope of those streaks shows that the flow patterns are moving from bottom to top since the streaks point in the same direction with increasing time. This behavior was expected because the schematic depiction in Fig. 1 shows the large-scale circulation of the flow, also pointing in the far-field region to the top.

The space-time plot along the horizontal dashed line of Fig. 4(a) is shown in Fig. 4(c). Also, along that line, periodic fluctuations seem to be indicated by the streak pattern. This means that those fluctuations spread over the entire width of the cell. However, no horizontal movement of those fluctuations can be seen at the same time since the pattern here is horizontal and not tilted.

Finally, Fig. 4(d) shows again the PSD of two positions within the FOV indicated by the star markers in Fig. 4(a). The red spectrum is, again, taken from a wall distance of $x = 30$ mm and can therefore be compared to the red spectrum in Fig. 3(d) since it was at the same distance but from another measurement. The comparison of those two spectra reveals some essential similarities, namely that both have two distinct peaks, one near a frequency of $f \approx 2 \times 10^{-2}$ Hz and a second at $f \approx 1 \times 10^{-1}$ Hz. The comparison of the space-time plots in Figs. 3(b) and 3(c) with those of Figs. 4(b) and 4(c) again suggests that the lower frequency peak originates from the far-field flow, while the peak at a higher frequency comes from the wall jet. The blue spectrum that shows that the frequency response even further away from the wall agrees with this interpretation since, in this spectrum, the peak at higher frequencies has disappeared. This suggests that the wall-jet fluctuation decays with increasing distance to the wall due to viscous friction. On the other hand, the peak in the lower frequency range is nearly identical to that from the red spectrum, showing that the underlying fluctuation is present at both wall distances.

For a more detailed investigation of the underlying physical processes that cause the specific frequencies found in the different measurements and wall distance positions, we analyze whether it is possible to relate those frequencies to the typical frequencies introduced in Sec. II. At first, we verify whether the high-frequency peak corresponding to the wall-jet flow characteristics relates to the wall-jet frequency found by Zhao *et al.* [35] and given in Eq. (1). In general, it would be possible just

to calculate the frequency as it was introduced. However, the boundary conditions of the current experiment are different from those of Zhao *et al.* [35] since they had a constant temperature difference $\Delta\vartheta$ between the sidewall and fluid, while the temperature difference in the current experimental setup is a function of the vertical coordinate $\Delta\vartheta(y)$. Therefore, it is necessary to find the best implementation scheme for the temperature difference for setups with changing temperature differences. The easiest implementation is to use the local temperature difference at the height of interest. However, it is conceivable that in regions where the temperature difference changes rapidly, the influence of the temperature difference from the upstream positions of the wall jet may play a more important role than the local temperature difference. For this reason, two different kinds of wall-jet frequencies were calculated for the current experiment and compared to the PSD from the PIV wall measurement.

The comparison between the wall measurement and the theoretical wall-jet frequencies is shown in Figs. 5(a)–5(c). The color plots in subfigures (a) and (b) show the PSD along a vertical axis at a wall distance of $x = 3$ mm for the vertical (v) and horizontal (u) velocity components, respectively. The red and dashed red lines show the theoretical local frequency of the wall jet using either a space-averaged or the local temperature difference for the calculation. For the calculation of the space-averaged temperature difference, all temperature differences from the starting point of the wall jet (top position of the vertical plate) down to the local position of interest were averaged. Using this procedure results in a local temperature difference but still considers the upstream positions of the wall jet. Applying the space-averaged temperature difference $\widehat{\Delta\vartheta}(y)$ to Eq. (1) results in a space-averaged wall-jet frequency $\widehat{f}_{\text{wj}}(y)$. The profiles of the local and the space-averaged temperature differences and the initial temperature profile of the wall measurement are shown for comparison in Fig. 5(c) along the dimensionless vertical coordinate (y/H). Since two counterdirected wall jets are present in the experimental setup, the deviation between the two types of temperature difference increases from the top and the bottom towards the middle position, respectively, since both wall jets stream towards the middle. It can be seen that, especially in the thermocline region, large differences occur between $\Delta\vartheta$ and $\widehat{\Delta\vartheta}$, also leading to increasing differences in the calculated wall-jet frequency.

Figure 5(a) can be seen as an extension of the black curve in Fig. 3(d) since it shows the spectra of the vertical velocity component not only for a height of $y = 500$ mm ($\hat{=}y/H = 0.67$) but also for all the other heights within the FOV. The color-coded values of the PSD show that the behavior of the wall jet is very similar over the entire

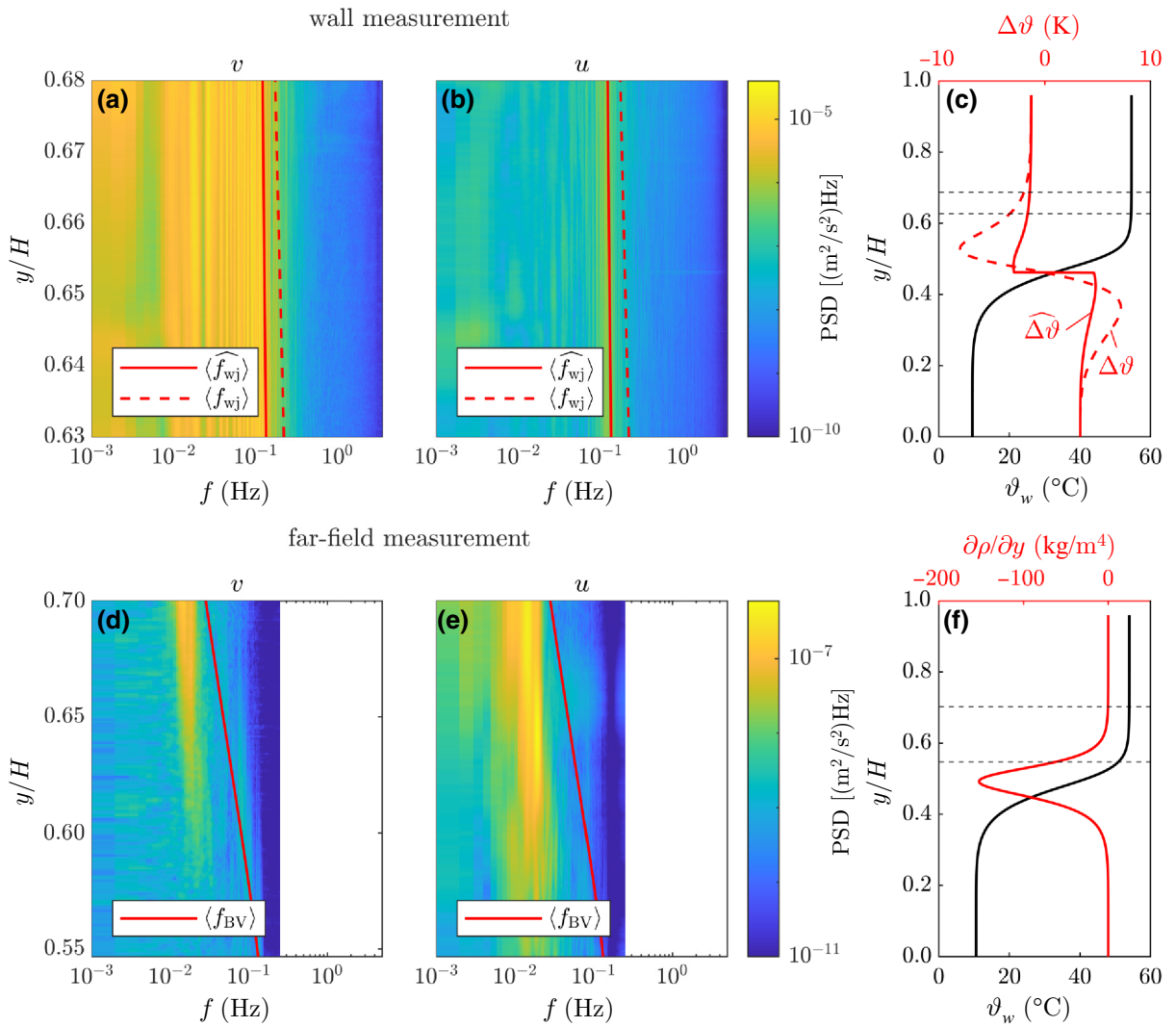


FIG. 5. Subfigures (a) and (b) show the PSD calculated for all time series at a wall distance of $x = 3$ mm for the vertical and the horizontal velocity components, respectively. Subfigure (c) shows the temperature profile measured at the beginning of the wall measurement in the water (black line) and the space-averaged and local temperature difference (red solid line and red dashed line) used to calculate the corresponding characteristic wall-jet frequencies \widehat{f}_{wj} and \widehat{f}_{wj} , respectively. Subfigures (d) and (e) show the PSD at a wall distance of $x = 100$ mm taken from the far-field measurement and again for the vertical and horizontal velocity components, respectively. Subfigure (f) shows the temperature profile (black line) at the beginning of the far-field measurement and the corresponding vertical density gradient of the water (red line) used to calculate the local BVF \widehat{f}_{BV} . The dashed lines in (c) and (f) show the lower and upper boundaries of the wall and far-field PIV measurements, respectively.

region, with high values in the low-frequency range indicated by yellow regions and then rapidly decreasing values towards higher frequencies. Interestingly, the border at which the decay seems to start coincides very well with the theoretical time-averaged wall-jet frequency \widehat{f}_{wj} calculated using the space-averaged temperature difference. In contrast, the line representing the time-averaged theoretical frequency \widehat{f}_{wj} using the local temperature difference deviates slightly from this border towards higher frequencies, suggesting that, indeed, the upstream part of the wall jet has a noticeable influence on the characteristic frequency of the flow. Figure 5(b) supports this observation

even better as it shows that in the spectra of the horizontal velocity component only one distinct peak can be found that again coincides very well with \widehat{f}_{wj} .

Since the characteristic frequency that was found by Zhao *et al.* [35] was described as the resonance frequency, which becomes dominant if the flow is subject to artificial perturbations and shows the transition from laminar to turbulent flow, it can be concluded that the natural convection flow of the current experiment is also in the transition state to turbulent flow. Interestingly, there was no need for artificial perturbations to cause periodic fluctuations. The reason for that might be that in a real-world experiment,

some small perturbations, e.g., in the form of tiny air bubbles, are present. These air bubbles are either attached to the wall and disturb the wall-jet flow or detach and rise to the surface, causing flow perturbations. However, the calculated characteristic frequency was the upper limit of dominant frequencies in the vertical velocity component, while it was the only dominant frequency in the horizontal velocity component. Concerning the application of TES, this finding is of high importance since Zhao *et al.* [35] have shown that the presence of the periodic flow fluctuations and the presence of transitional flow enhances heat transfer by up to 44%, which can lead to both increased heat loss to the surroundings of the TES and increased heat transfer from the hot to the cold layer of the thermal stratification and thus to decreasing exergy content of the TES. Therefore, the calculation of the characteristic frequency \hat{f}_{wj} provides, in combination with a velocity estimation of the vertical wall jet (see Ref. [28]), a relatively easy estimation of the flow state, needing only the relevant fluid properties as well as the wall and fluid temperatures.

Regarding different storage tank materials and thicknesses, it is worth mentioning that those parameters are all covered in the local temperature difference between the sidewall and the fluid, since it was shown in a scaling analysis by the authors [28] that the wall-jet velocity scales roughly with the square root of this temperature difference and the reciprocal of the square root of the local downstream position of the wall jet. Using this information, one can estimate the wall-jet behavior for different kinds of TES. For instance, with decreasing thermal diffusivity in the sidewall (i.e., stainless steel, concrete), the temperature difference also decreases, leading to lower flow velocities and, therefore, fewer fluctuations. However, for large-scale TES, the velocities of the wall jets increase with increasing length of the vertical sidewall. Additionally, for TES with higher storage temperatures like molten salt storage, the temperature difference between the wall and fluid also increases, leading to stronger fluctuations.

After the deeper investigation of the wall-jet fluctuation using the upper row of Fig. 5, subfigures (d)–(f) provide a deeper insight into the fluctuations of the far-field region. Figures 5(d) and 5(e) show the PSD along a vertical axis at $x = 100$ mm calculated from the far-field measurement data. For better comparison to the spectra of the wall measurement, the frequency axis is the same as in subfigures (a) and (b), even though the spectra end at lower frequencies due to the lower sampling frequency (see Table I). Figure 5(f) shows the initial temperature profile (black line) after the filling of the model experiment for this measurement and the corresponding vertical density gradient $\partial\rho/\partial y$ that is needed for the calculation of the BVF that is expected to occur in the far-field region. The progression of the red curve shows that, within the FOV (indicated by the two horizontal dashed lines), the gradient strongly increases from top to bottom. This also suggests

a noticeable increase in the BVF since it scales with the square root of the density gradient. The calculated vertical profile of the BVF $\langle f_{BV} \rangle$ is shown by a red line in subfigures (d) and (e) to see whether the PIV measurement can verify this expectation. The angled brackets again indicate the time averaging over the measuring period.

The color-coded PSD of the vertical velocity component shows a yellow region for the FOV's upper part, indicating a distinct peak in those spectra. However, moving further down, this peak in the spectra disappears, leaving only a light blue region that does not represent one characteristic frequency in this lower region. In contrast to the wall measurement, the expected theoretical frequency profile of the BVF does not match the peaks of the spectra originating from the PIV measurement. Instead, the profile of $\langle f_{BV} \rangle$ suggests slightly higher dominant frequencies. Moreover, the BVF profile is tilted towards higher frequencies in the bottom region because of the already-mentioned increasing density gradients in the lower part of the FOV. Even though the peak region of the color-coded PIV spectra is also slightly tilted in the same direction, the tilt has a much steeper slope than the theoretical frequency profile.

The spectra of the horizontal velocity component in Fig. 5(e) look similar to those of the vertical component since the light yellow regions in the upper part are in the same position, showing the peaks of those spectra. However, a major difference between the two velocity components is that the fluctuation amplitude in u is higher, resulting in higher values of the PSD (indicated by lighter yellow regions). Also, the decay of the distinct peak region of the spectra is less evident since the yellow region of the horizontal component extends much further to the bottom of the FOV (this is still true for the normalized PSD spectra, which are not shown here). Those observations suggest that the horizontal velocity component is less damped, leading to a wider spreading of its fluctuations. This is because the thermal stratification dampens vertical fluid displacements since a displaced fluid parcel experiences a restoring force that increases with higher density gradients. On the other hand, there are nearly no density gradients in the horizontal direction that could cause a similar restoring force so that the horizontal velocity component is damped only by viscous forces (which, of course, also act on the vertical velocity component).

Overall, the presented results on the far-field fluctuations do not allow a clear assignment of the observed velocity fluctuations to the BVF because the theoretical frequency estimation deviates from the peaks in the measured spectra. For this reason, the far-field fluctuations are investigated over a more comprehensive vertical range to get a deeper insight into the physical processes and their dependence on the vertical position within the thermal stratification. However, since another PIV investigation is unsuitable for investigating a much larger FOV with

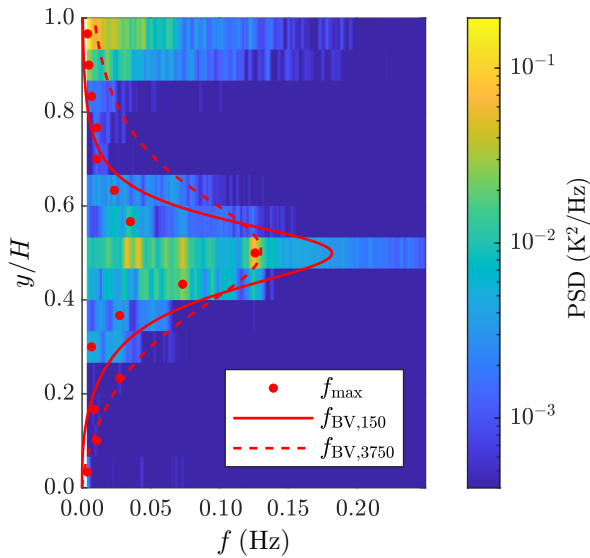


FIG. 6. Space-frequency illustration of the 15 thermocouples' PSD spectra during the additional temperature measurement. The red solid and dashed lines show the development of the BVF from the beginning ($t = 150$ s) to the end ($t = 3750$ s) of the investigated time series and the red dots show the frequency of maximum PSD for all spectra.

sufficient spatial resolution, an additional experiment was performed using only the temperature sensors in the water at an increased sampling frequency of 1 Hz.

Figure 6 shows the results of the spectral analysis of the additional temperature measurement with a wall distance of the sensors of $x \approx 190$ mm. At first, the moving median with a window size of 300 samples ($=300$ s) was subtracted from each time series, resulting in temperature time series that contained only fluctuations but not the general temperature trend across the measuring period. The final time series of the temperature fluctuations cover a period of 3600 s starting at $t = 150$ s and ending at $t = 3750$ s since the moving median cannot be calculated in the first time steps with its entire window size and would therefore influence the resulting time series. Finally, the PSD was calculated for all 15 sensors from the preprocessed time series using *Welch's* method [46] and plotted as a color-coded space-frequency diagram showing the vertical position and the frequency range of the PSD spectra. The lower bound of the color map was set to $4 \times 10^{-4} \text{ K}^2 \text{ Hz}^{-1}$ since the values below cannot be distinguished from measurement noise (according to the mentioned precision of the temperature sensors in Sec. III). In addition, the BVF profiles from the beginning $f_{\text{BV},150}$ and at the end $f_{\text{BV},3750}$ of the time series are plotted to show the temporal development of the theoretical frequency profile due to the vertically extending thermocline. The red dots represent the frequencies at which the 15 spectra reach their maxima.

The color plot shows that large parts of the space-frequency map are related to sensor noise, as those regions

appear in dark blue. This is especially true for the higher-frequency range but also for lower frequencies in the bottom part of the model experiment. Therefore, relevant values of the PSD can only be found in the middle and at the upper end of the experiment. Also, between those two regions, the spectra show higher values in a relatively narrow frequency range around $f \approx 1 \times 10^{-2}$ Hz. The reason for the conspicuous PSD spectra of the upper two sensors is that those sensors are placed near the position where the temperature rod enters the experimental facility through a hole in the top panel, and increased heat losses to the surroundings take place. Those losses lead to temperature changes in the water and, therefore, to buoyancy effects and fluctuations. However, the dominant frequency of those two spectra is between the two BVF profiles, suggesting that the fluctuations are initiated in various frequencies but result in periodic fluid oscillations that can be described with the BVF.

The spectra further downwards show that the relevant parts are broadening with increasing density gradients, reaching the maximum width right in the middle where the density gradient also has its extreme point [see also Fig. 5(f)]. This position coincides with the highest frequencies found in the two BVF profiles since those also depend on the density gradient. Therefore, the theoretical profiles form an upper cutoff frequency above which the spectra of the measured temperatures rapidly decrease. However, in contrast to the two sensors at the top, the dominant frequencies of the spectra in the middle seem unrelated to the theoretical BVF profiles. They show higher deviations towards lower frequencies compared to the BVF profiles the further they are in the thermocline region. The main peak in the PSD of the sensor right in the middle seems to be an exception since it lies very close to the profile of $f_{\text{BV},150}$. However, two more peaks in that spectrum are indicated by yellow areas at $f \approx 3.5 \times 10^{-2}$ Hz and $f \approx 7 \times 10^{-2}$ Hz from which the first corresponds very well to the trend of the dominant frequencies of the two sensors above. The main peak at a frequency of $f \approx 1.25 \times 10^{-1}$ Hz is related to one certain event in the time series (presumably caused by a rising air bubble since it was also visible in the adjacent sensors' time series), leading to an oscillation of the fluid layer at a frequency near its BVF.

On the other hand, the slightly lower peaks are assumed to be caused by the propagation of the oscillation of adjacent fluid layers (mainly from those above the central sensor). An explanation for this propagation is that the fluid oscillation in regions with lower fluid density gradients can have higher amplitudes since the restoring buoyancy force is lower than in the center of the thermocline. Because of the higher amplitudes of the oscillation, the corresponding BVF of the fluid layer where the oscillation originates from can then propagate into fluid layers with different density gradients. However, the oscillations

amplified directly in those regions cannot propagate that deep into other layers since their amplitudes are lower due to the high restoring buoyancy force in that region. This behavior finally leads to the effect that the frequencies originating from regions where density gradients are present but relatively low propagate the most. Comparing this assumption with the results from Fig. 6 shows that, indeed, the frequency from the sensor at $y/H = 0.76$ seems to propagate downwards, crossing the theoretical profile of $f_{BV,3750}$ and slightly increasing its oscillation frequency the further it enters the thermocline region.

V. COMPARISON TO LARGE-SCALE THERMAL ENERGY STORAGE

In this section, a measurement performed in a large-scale experiment of a stratified TES is analyzed and compared to the previous results from the small-scale model experiment. The data for this comparison come from the *Test facility for thermal Energy Storage In molten Salt* (TESIS) located at the German Aerospace Center (DLR) in Cologne. The overall facility consists of two subfacilities, the *TESIS:com* facility, used for component tests, and the *TESIS:store* facility, a test TES tank [47,48]. The latter was used to perform the experiment presented in the following.

The *TESIS:store* storage tank has a height of $H_s = 6$ m, a diameter of $D = 2.2$ m, and can hold a liquid volume of up to 22 m^3 . A schematic depiction of the *TESIS:store* tank is shown in Fig. 7(a). In the presented experiment, only liquid storage material, namely, the so-called *solar salt*, a eutectic, nitrate-based molten salt mixture (60% $\text{NaNO}_3 + 40\%$ KNO_3) specifically optimized for concentrated solar power plants, was used [49–51]. However, the facility can also be used as a packed-bed TES utilizing a solid filler material [52]. In the present study, the storage tank was filled by half with hot ($\vartheta_{s,\max} \approx 550 \text{ }^\circ\text{C}$) solar salt before a small layer of cold ($\vartheta_{s,\min} \approx 300 \text{ }^\circ\text{C}$) fluid was filled below the hot layer, creating a thermally stratified system. After that, the measurement of the standby period started with a total measurement period of 10 h (= 36 000 s). The three-dimensional temperature distribution was recorded using an array of type-K thermocouples to measure a vertical temperature profile and the radial temperature distribution at various heights. Yellow dots indicate the sensors' positions in this study in the schematic.

Figure 7(b) shows the vertical temperature distribution of the stratified solar salt at the beginning and the end of the experiment (black lines). As can be seen, the tank was filled up to a height of $z = 3.5$ m, from which everything above $z = 1$ m was part of the hot, isothermal region of the stratification. The thermocline region extends from $0 \leq z \leq 1$ m, and only a relatively thin layer at the bottom of the tank contains cold isothermal fluid. Over time, the thermocline extends, especially in this bottom region, and

the temperature in the upper isothermal area decreases due to losses to the surrounding. The corresponding density gradients of the stratification are shown as red lines (using the upper, red x axis). The highest gradients are reached in the upper part of the thermocline region. Those high gradients decrease over time, and due to the extent of the thermocline region towards the bottom, there are regions in which the density gradient increases.

Figure 7(c) shows the resulting PSD spectra of the 26 vertically aligned thermocouples as a space-frequency plot in the same manner as it was shown for the model experiment in Fig. 6. Although the *TESIS:store* facility is entirely different from the model experiment, with a much higher volume, different storage fluid, larger characteristic length (i.e., a different height that can influence the velocity and flow state of the natural convection along the vertical side-walls), different geometry, and a higher temperature range, it still behaves relatively similar in terms of its far-field fluctuations. The plot shows that the fluctuations in the upper isothermal part are limited to a relatively low and narrow frequency range that also have low amplitudes. In this region, the two profiles of the BVF frequency fluctuate because of the uncertainty in the temperature measurement, which becomes even more apparent in the resulting density gradient and BVF. However, in the thermocline's upper region, both the spectra and the theoretical BVF profiles start extending towards higher frequencies so that the BVF profiles form an upper cutoff frequency again. Also, similar to the model experiment investigations, the main peaks of the spectra (f_{\max}) are at much lower frequencies. Moreover, this measurement shows even better than the measurement in the model experiment that the highest amplitudes in the space-frequency plot occur in the upper part of the thermocline, supporting the assumption from the last section that the oscillations from the thermocline bounds propagate into the thermocline region, causing the most noticeable fluctuations.

The depiction of the fluctuation behavior in Fig. 7(d) supports this statement since the red line shows the standard deviation of the vertically aligned thermocouples' time signals. While in the upper region (apart from the uppermost sensor, which is directly under the free surface of the fluid) only negligible temperature fluctuations occur, the standard deviation drastically increases in the upper thermocline region, suggesting that the internal flow perturbs the thermocline, leading to higher temperature fluctuations. The standard deviation decreases towards the bottom since the density gradient also decreases. It is likely that the damping effect of the restoring buoyancy forces suppresses fluid flow in this region before it can lead to strong fluctuations.

Another interesting fact is shown by the black line that shows the standard deviation of the horizontally aligned thermocouples at a height of $z = 0.75$ m (black line and axes). The line shows that the fluctuation of the stratified

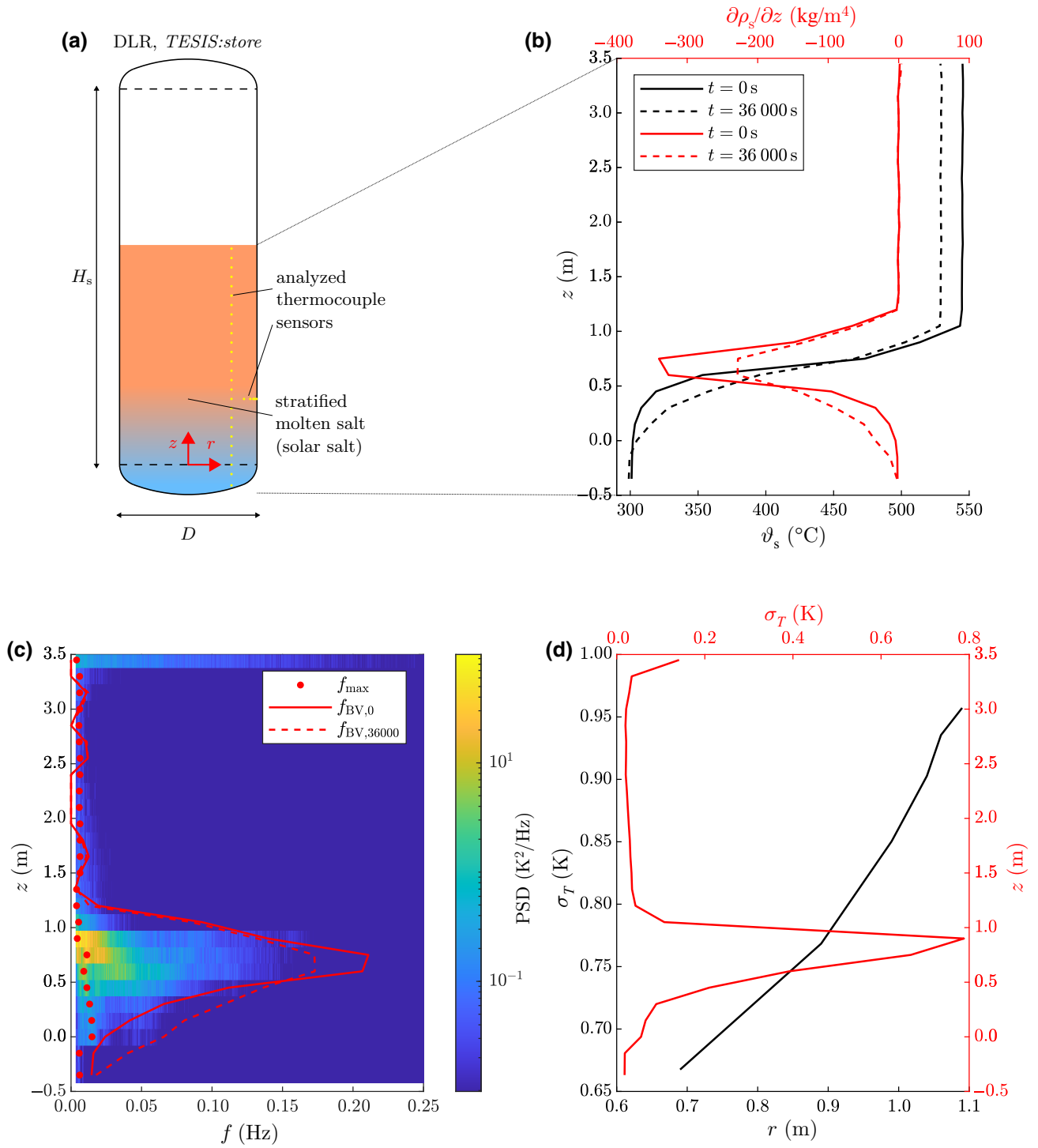


FIG. 7. (a) Schematic depiction of the *TESIS:store* TES test facility as part of the *TESIS* facility at the German Aerospace Center (DLR) in Cologne, Germany. The sketch shows the relative dimensions, the origin of the cylindrical coordinate system, and the positions of the used sensors. (b) Vertical temperature distribution $\vartheta_s(z)$ (black lines) inside the TES facility at the beginning (solid line) and the end (dashed line) of the measuring period. The red lines show the corresponding vertical density gradient $\partial\rho_s/\partial z(z)$ of the temperature distribution. (c) Space-frequency plot of the PSD of the vertically aligned temperature sensors [see (a)] with red dots indicating their maxima. The red solid and dashed lines show the theoretical BVFs at the beginning and the end of the measuring period, respectively. (d) Standard deviation of all utilized temperature sensors where the black line (and the corresponding black axis) shows the standard deviation of the horizontally aligned sensors at a height of $z = 0.75$ m, and the red line (and the red axis) shows the standard deviation of the vertically aligned sensors at the radius $r = 0.69$ m.

fluid is less for smaller r , i.e., with a higher distance to the vertical sidewall ($r = 1.1$ m). This clearly shows that perturbation of the fluid layers originates from the sidewall. This effect seems logical since the heat losses to the surroundings, and the axial wall conduction in the sidewall, lead to natural convection in the adjacent fluid layers. This convection flow is expected to stream from top to bottom since both mentioned heat transfer processes cause the near-wall fluid layer to cool down. The downward-directed wall jet then disturbs the stable stratification and initiates the periodic oscillation of the fluid, which finally results in the observed fluctuations. The driving mechanism decreases with further distance to the wall, and the fluctuation is more damped due to viscous forces.

Overall, the measurement in the *TESIS:store* facility has proven that the observed physical phenomena in the small-scale model experiment also appear in a large-scale facility despite all the major differences between the two experiments. Despite the fact that no velocity measurements could be performed, the near-wall flow seems strong enough to fuel relevant fluctuations detected by the temperature measurements.

VI. CONCLUSION

In this paper, we investigated the temporal behavior of natural convection flows inside different stratified TES systems. In detail, in a previous time-averaged study, fluctuating behavior of wall jets adjacent to the vertical sidewalls of a TES system was observed, which we aimed to characterize in more detail.

For this reason, PIV experiments were performed in a small-scale model experiment in two regions, the near-wall region and across the entire width of the experimental setup. The time-resolved PIV data were further analyzed using space-time plots and frequency analysis. In the near-wall region, it was found that the wall jet exhibits a relatively high frequency of about 1×10^{-1} Hz. A characteristic frequency of about 2×10^{-2} Hz was observed in the far field. The transition region between the wall jet and the far field showed both characteristic frequencies in its power spectral density estimates.

A comparison with an adjusted empirical formulation for the characteristic frequency in vertical natural convection, which was found to be characteristic of the transition from laminar to turbulent flow, agreed very well with the frequency response of the PIV data. The original equation was developed in an experiment with an isothermal sidewall and a constant temperature difference between that wall and the adjacent fluid. Since in the experiment of this study the temperature difference depends on the height, the equation was adjusted by using a space-averaged temperature difference calculated from the upstream part of the studied wall jet and can be used for the estimation of typical frequencies in real-scale TES.

In the far field the observed characteristic frequency was compared to the BVF, typical for density-stratified fluids. The vertical profile of the theoretical frequency was found to build an upper cutoff frequency for the spectra of the PIV measurement. However, the dominant frequency from the PIV spectra did not coincide with the theoretical profile. To further evaluate the effect on the heat transfer, long-time measurements were performed using temperature sensors placed in the far field of the sidewall and equally distributed over the entire model experiment's height. The results have shown that in regions of relatively low density gradients, which correspond in stratified TES to the upper and lower bounds of the thermocline, the frequencies match with the theoretical BVF. Since, in those regions, the restoring buoyancy forces that act on vertically displaced fluid parcels are low, the fluctuations at this frequency have large amplitudes and thus enhance mixing. These disturbances also propagate into deeper regions of the thermocline, which is the reason that the dominant frequencies inside the thermocline region are lower compared to the theoretical BVF that one would expect. These fluctuations are detrimental to both the energy and exergy efficiencies of the system. Firstly, the heat transfer to the sidewalls is increased, which results in a higher energy loss to the surrounding and, furthermore, in an increased heat transfer due to conduction in the sidewalls. Secondly, the fluctuations enhance mixing inside the thermocline region, which results in exergy loss.

The long-time temperature measurement of a real-scale molten-salt TES showed very similar behavior concerning the previously described frequencies. Moreover, it was shown that the fluctuations are induced in the sidewall region, probably due to natural convective flows resulting from heat transfer processes that occur in this region. The good agreement between the results of the model experiment ($V = 0.1$ m³, $\vartheta = 10$ °C–60 °C) and the large-scale ($V = 22$ m³, $\vartheta = 300$ °C–550 °C) facility emphasizes that the physical phenomena are similar, can be described with the developed models, and have to be considered when increasing the scale of TES.

To improve the efficiency of larger stratified TES as necessary for Carnot batteries, different measures can be taken. The improvement of the insulation to the surroundings lowers energy losses and thus increases the storage time. However, since vertical heat transfer dominates, then exergy is lost considerably faster by mixing. A possible solution to that problem is the placement of insulation on the inner side, which prevents heat transfer to the surrounding and in the vertical direction. However, here low-cost materials have to be identified to withstand high temperatures, corrosion due to storage materials, and to withstand thousands of thermal cycles. Another option is the suppression of the flow in the near-wall region, where porous materials may be used to separate the thermal and momentum boundary layers. Since the strongest fluctuations of

both systems originate from the thermocline’s upper and lower boundaries, it is clear that preventing mixing, e.g., by floating barriers in these regions, is crucial for the sustained exergetic efficiency of the TES. However, here the same requirements concerning the materials have to be met.

Future fundamental research and field tests are necessary for larger scales, higher temperature levels also promoting radiation, different materials, and geometries to develop highly efficient (energy and exergy) TES.

ACKNOWLEDGMENTS

The authors gratefully acknowledge the group from DLR Cologne and Stuttgart, especially André Thess, Annelies Vandersickel, and Thomas Bauer for providing the data of the real-scale TES system *TESIS* and for fruitful discussions that significantly contributed to this paper. Moreover, Alexander Thieme and Wladislaw Seiferth are acknowledged for their great support in setting up the experiment. Financial support from the German Research Foundation within the priority programme 2403

‘Carnot Batteries’ under Grant No. CI 185/15-1 is gratefully acknowledged.

APPENDIX A: FLOW-FIELD SNAPSHOTS

Figure 8 shows a series of ten consecutive snapshots of the near-wall flow that was also shown in Fig. 3(a). Subfigures (a)–(j) show the time steps t_1 to t_{10} that are separated by 1 s. As can be seen, a vortexlike structure is moving from top to bottom during this period of flow. The fact that the flow structure is a vortex becomes clear due to the vector arrows showing a circular shape in the border region between upward-directed and downward-directed flow (border between the blue and yellow areas). This event is visualized in a short video [53,54].

APPENDIX B: DETAILED SPECTRA

Figure 9 shows partial spectra of the black spectrum in Fig. 3(d). The four subspectra result from splitting the time series of the temperature into four parts of equal length and computing the spectrum for each individual period.

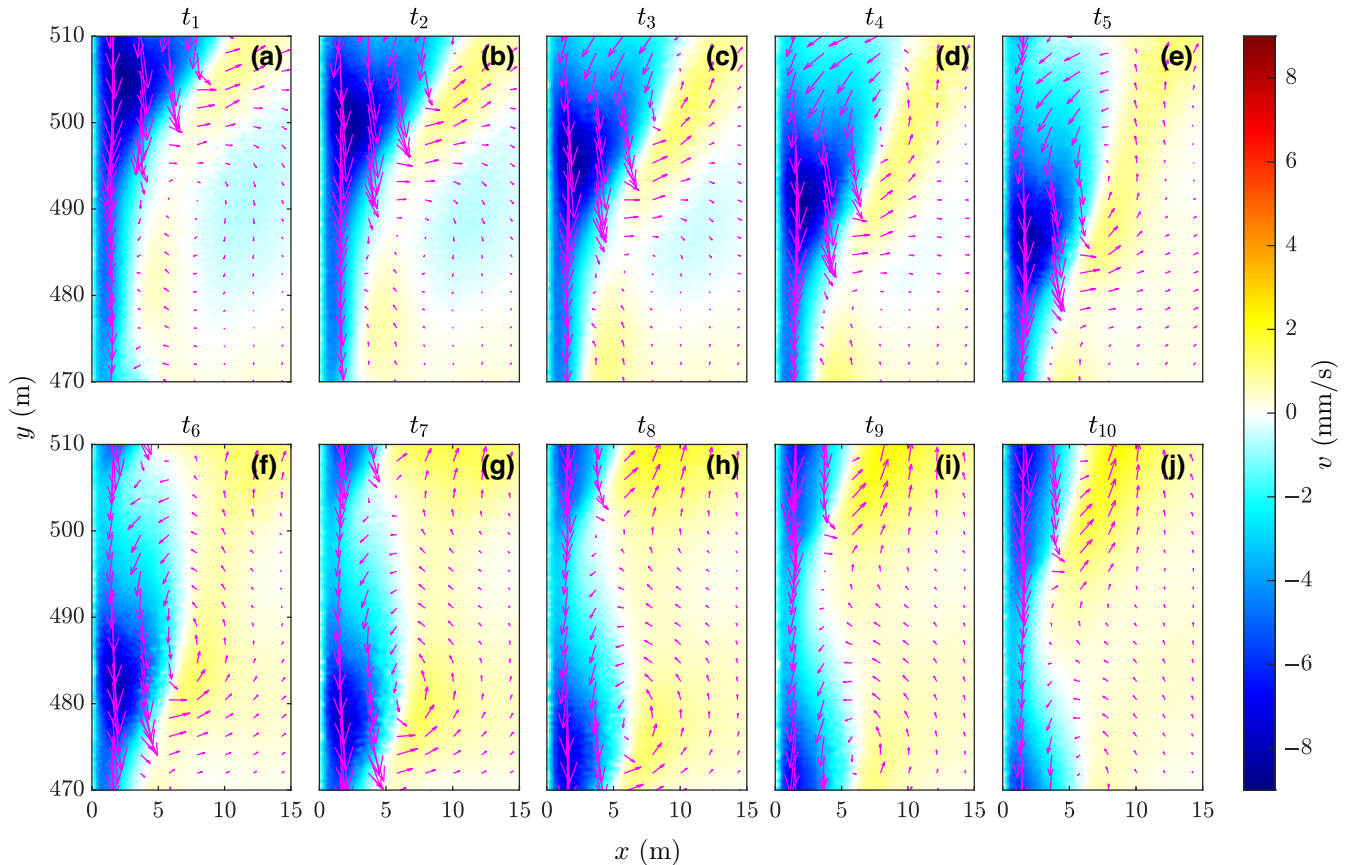


FIG. 8. The subfigures (a)–(j) show a series of consecutive temporal snapshots of the flow field in the near-wall region with a time difference of one second between the snapshots. The colored background shows the vertical velocity component v with the corresponding color bar on the right. The arrows show every 15th vector in both the horizontal and the vertical direction, respectively. Subfigure (e) shows the same snapshot as Fig. 3(a).

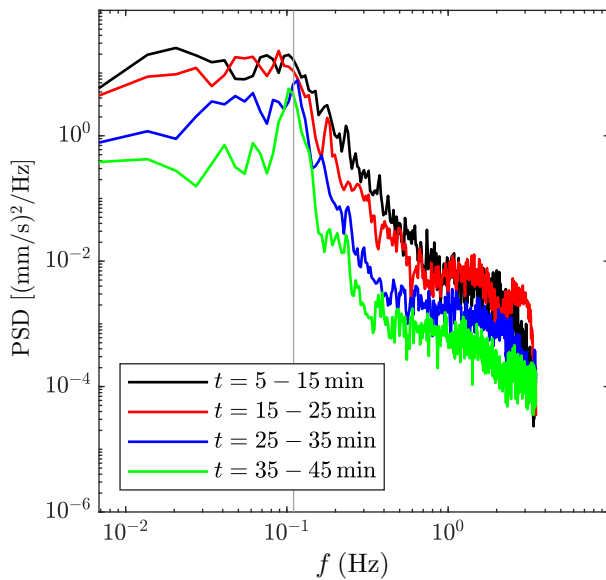


FIG. 9. Partial spectra of the black spectrum in Fig. 3(d) ($x = 3$ mm, $y = 500$ mm) as a result of splitting the corresponding time series into four equally long parts of 10 min each. The vertical gray line indicates the peak frequency of $f = 1.1 \times 10^{-1}$ Hz.

The spectra show that the flow needs about 25 min for the dominant frequency (indicated by the gray line) to become clearly visible in the spectra. However, this dominant frequency is already in the first (black) spectrum, the upper cutoff frequency over which the spectrum decreases rapidly.

[1] A. Olabi, C. Onumaegbu, T. Wilberforce, M. Ramadan, M. A. Abdelkareem, and A. H. Al – Alami, Critical review of energy storage systems, *Energy* **214**, 118987 (2021).

[2] H. Chen, T. N. Cong, W. Yang, C. Tan, Y. Li, and Y. Ding, Progress in electrical energy storage system: A critical review, *Prog. Nat. Sci.* **19**, 291 (2009).

[3] D. Pérez-Gallego, J. Gonzalez-Ayala, A. Calvo Hernández, and A. Medina, Thermodynamic performance of a Brayton pumped heat energy storage system: Influence of internal and external irreversibilities, *Entropy* **23**, 1564 (2021).

[4] J. Gonzalez-Ayala, D. Salomone-González, A. Medina, J. Roco, P. Curto-Risso, and A. Calvo Hernández, Multicriteria optimization of Brayton-like pumped thermal electricity storage with liquid media, *J. Energy Stor.* **44**, 103242 (2021).

[5] O. Dumont, G. F. Frate, A. Pillai, S. Lecompte, M. Depaepe, and V. Lemort, Carnot battery technology: A state-of-the-art review, *J. Energy Stor.* **32**, 101756 (2020).

[6] A. Benato, Performance and cost evaluation of an innovative pumped thermal electricity storage power system, *Energy* **138**, 419 (2017).

[7] A. Benato and A. Stoppato, Pumped thermal electricity storage: A technology overview, *Therm. Sci. Eng. Prog.* **6**, 301 (2018).

[8] X. Luo, J. Wang, M. Dooner, and J. Clarke, Overview of current development in electrical energy storage technologies and the application potential in power system operation, *Appl. Energy* **137**, 511 (2015).

[9] T. Yang, W. Liu, G. J. Kramer, and Q. Sun, Seasonal thermal energy storage: A techno-economic literature review, *Renew. Sustainable Energy Rev.* **139**, 110732 (2021).

[10] R. Georgious, R. Refaat, J. Garcia, and A. A. Daoud, Review on energy storage systems in microgrids, *Electronics* **10**, 2134 (2021).

[11] G. Alva, Y. Lin, and G. Fang, An overview of thermal energy storage systems, *Energy* **144**, 341 (2018).

[12] L. Geissbühler, M. Kolman, G. Zanganeh, A. Haselbacher, and A. Steinfeld, Analysis of industrial-scale high-temperature combined sensible/latent thermal energy storage, *Appl. Therm. Eng.* **101**, 657 (2016).

[13] H. Mahon, D. O'Connor, D. Friedrich, and B. Hughes, A review of thermal energy storage technologies for seasonal loops, *Energy* **239**, 122207 (2022).

[14] R. Bayón, E. Rivas, and E. Rojas, Study of thermocline tank performance in dynamic processes and stand-by periods with an analytical function, *Energy Proc.* **49**, 725 (2014).

[15] J. Marti, L. Geissbühler, V. Becattini, A. Haselbacher, and A. Steinfeld, Constrained multi-objective optimization of thermocline packed-bed thermal-energy storage, *Appl. Energy* **216**, 694 (2018).

[16] N. Calvet, J. C. Gomez, A. Faik, V. V. Roddatis, A. Mefre, G. C. Glatzmaier, S. Doppiu, and X. Py, Compatibility of a post-industrial ceramic with nitrate molten salts for use as filler material in a thermocline storage system, *Appl. Energy* **109**, 387 (2013).

[17] J. van Berkel, C. C. M. Rindt, and A. A. van Steenhoven, Thermocline dynamics in a thermally stratified store, *International Journal of Heat and Mass Transfer* (2002).

[18] S. Göppert, T. Urbaneck, U. Schirmer, R. Lohse, and B. Platzer, Be- und entladesysteme für thermische schichtenspeicher: Teil 1 – überblick, *Chem. Ing. Tech.* **80**, 287 (2008).

[19] R. Lohse, S. Göppert, C. Kunis, T. Urbaneck, U. Schirmer, and B. Platzer, Be- und entladesysteme für thermische schichtenspeicher: Teil 2 – untersuchungen des beladeverhaltens, *Chem. Ing. Tech.* **80**, 935 (2008).

[20] R. Lohse, T. Urbaneck, C. Brämer, and B. Platzer, Effects during loading of hot water storages with a high aspect ratio, *EuroHeat&Power* **9**, 42 (2012).

[21] E. García-Marí, M. Gasque, R. P. Gutiérrez-Colomer, F. Ibáñez, and P. González-Altozano, A new inlet device that enhances thermal stratification during charging in a hot water storage tank, *Appl. Therm. Eng.* **61**, 663 (2013).

[22] H. Taheri, F. P. Schmidt, and M. Gabi, Numerical investigation of effective heat conductivity of fluid in charging process of thermal storage tank, *Open J. Fluid Dyn.* **05**, 39 (2015).

[23] K. Manu, P. Anand, U. K. Chetia, and S. Basu, Effects of instabilities and coherent structures on the performance of a thermocline based thermal energy storage, *Appl. Therm. Eng.* **87**, 768 (2015).

- [24] A. Tinaikar, S. Advaith, U. K. Chetia, K. Manu, and S. Basu, Spatio-temporal disruption of thermocline by successive laminar vortex pairs in a single tank thermal energy storage, *Appl. Therm. Eng.* **109**, 924 (2016).
- [25] S. Advaith, K. V. Manu, A. Tinaikar, U. K. Chetia, and S. Basu, Interaction of vortex ring with a stratified finite thickness interface, *Phys. Fluids* **29**, 093602 (2017).
- [26] H. Khurana, R. Majumdar, and S. K. Saha, Thermal stratification characteristics during simultaneous charging and discharging for different storage tank geometries with immersed discharging coil, *Appl. Therm. Eng.* **225**, 120235 (2023).
- [27] H. Otto, C. Resagk, and C. Cierpka, Optical measurements on thermal convection processes inside thermal energy storages during stand-by periods, *Optics* **1**, 155 (2020).
- [28] H. Otto and C. Cierpka, Influence of thermal stratification on vertical natural convection—experimental investigations on the example of thermal energy storage systems, *Phys. Fluids* **33**, 13 (2021).
- [29] R. J. Shyu and C. K. Hsieh, Unsteady natural convection in enclosures with stratified medium, *J. Sol. Energy Eng.* **109**, 127 (1987).
- [30] R.-J. Shyu, J.-Y. Lin, and L.-J. Fang, Thermal analysis of stratified storage tanks, *J. Sol. Energy Eng.* **111**, 54 (1989).
- [31] J. E. B. Nelson, A. R. Balakrishnan, and S. S. Murthy, Parametric studies on thermally stratified chilled water storage systems, *Applied Thermal Engineering* (1999).
- [32] E. Papanicolaou and V. Belessiotis, Transient hydrodynamic phenomena and conjugate heat transfer during cooling of water in an underground thermal storage tank, *J. Heat Transfer* **126**, 84 (2004).
- [33] Y. Jaluria and B. Gebhart, Stability and transition of buoyancy-induced flows in a stratified medium, *J. Fluid Mech.* **66**, 593 (1974).
- [34] J. C. Patterson and S. W. Armfield, Transient features of natural convection in a cavity, *J. Fluid Mech.* **219**, 469 (1990).
- [35] Y. Zhao, C. Lei, and J. C. Patterson, Resonance of the thermal boundary layer adjacent to an isothermally heated vertical surface, *J. Fluid Mech.* **724**, 305 (2013).
- [36] Y. Zhao, C. Lei, and J. C. Patterson, A PIV measurement of the natural transition of a natural convection boundary layer, *Exp. Fluids* **56**, 9 (2015).
- [37] B. Gebhart and R. Mahajan, Characteristic disturbance frequency in vertical natural convection flow, *Int. J. Heat Mass Transf.* **18**, 1143 (1975).
- [38] J. van Berkel, Mixing in thermally stratified energy stores, *Sol. Energy* **58**, 203 (1996).
- [39] S. S. Ratnu and K. V. Manu, Three-dimensional thermocline dynamics in thermal storage tanks, *J. Appl. Fluid Mech.* **14**, 1483 (2021).
- [40] K. Manu, P. Deshmukh, and S. Basu, Rayleigh–Taylor instability in a thermocline based thermal storage tank, *Int. J. Therm. Sci.* **100**, 333 (2016).
- [41] Y. Yen Kee, Y. Asako, T. Lit Ken, and N. A. Che Sidik, Uncertainty of temperature measured by thermocouple, *J. Adv. Res. Fluid Mech. Therm. Sci.* **68**, 54 (2020).
- [42] C. J. Kähler, S. Scharnowski, and C. Cierpka, On the uncertainty of digital PIV and PTV near walls, *Exp. Fluids* **52**, 1641 (2012).
- [43] C. Cierpka, S. Scharnowski, and C. J. Kähler, Parallax correction for precise near-wall flow investigations using particle imaging, *Appl. Opt.* **52**, 2923 (2013).
- [44] C. J. Kähler, T. Astarita, P. P. Vlachos, J. Sakakibara, R. Hain, S. Discetti, R. La Foy, and C. Cierpka, Main results of the 4th international PIV challenge, *Exp. Fluids* **57**, 97 (2016).
- [45] C. J. Kähler, S. Scharnowski, and C. Cierpka, On the resolution limit of digital particle image velocimetry, *Exp. Fluids* **52**, 1629 (2012).
- [46] P. Welch, The use of fast Fourier transform for the estimation of power spectra: A method based on time averaging over short, modified periodograms, *IEEE Trans. Audio Electroacoust.* **15**, 70 (1967).
- [47] N. Breidenbach, C. Martin, H. Jockenhöfer, and T. Bauer, Thermal energy storage in molten salts: Overview of novel concepts and the DLR test facility TESIS, *Energy Proc.* **99**, 120 (2016).
- [48] C. Odenthal, F. Klasing, and T. Bauer, Demonstrating cost effective thermal energy storage in molten salts: DLR’s TESIS test facility, *Energy Proc.* **135**, 14 (2017).
- [49] T. Bauer, C. Odenthal, and A. Bonk, Molten salt storage for power generation, *Chem. Ing. Tech.* **93**, 534 (2021).
- [50] A. Bonk, S. Sau, N. Uranga, M. Hernaiz, and T. Bauer, Advanced heat transfer fluids for direct molten salt line-focusing CSP plants, *Prog. Energy Combust. Sci.* **67**, 69 (2018).
- [51] T. Bauer, N. Pflieger, N. Breidenbach, M. Eck, D. Laing, and S. Kaesche, Material aspects of solar salt for sensible heat storage, *Appl. Energy* **111**, 1114 (2013).
- [52] C. Odenthal, F. Klasing, P. Knödler, S. Zunft, and T. Bauer, in *SOLARPACES 2019: International Conference on Concentrating Solar Power and Chemical Energy Systems* (Daegu, South Korea, 2020), p. 190025.
- [53] See Supplemental Material at <http://link.aps.org/supplemental/10.1103/PRXEnergy.2.043001> for a short video that visualizes the flow field.
- [54] H. Otto, C. Naumann, and C. Cierpka (2023), <https://doi.org/10.5281/zenodo.8271934>.